

# **ARTICLE**



1

https://doi.org/10.1038/s41467-022-29237-0

**OPEN** 

# Spin-orbit enabled all-electrical readout of chiral spin-textures

Imara Lima Fernandes 

1 

Note that Stefan Blügel 

1 

Note that Samir Lounis 

1,2 

Note that Stefan Blügel 

1 

Note that Samir Lounis 

1,2 

Note that Stefan Blügel 

1 

Note that Stefan Blügel 

Note

Chirality and topology are intimately related fundamental concepts, which are heavily explored to establish spin-textures as potential magnetic bits in information technology. However, this ambition is inhibited since the electrical reading of chiral attributes is highly non-trivial with conventional current perpendicular-to-plane (CPP) sensing devices. Here we demonstrate from extensive first-principles simulations and multiple scattering expansion the emergence of the chiral spin-mixing magnetoresistance (C-XMR) enabling highly efficient all-electrical readout of the chirality and helicity of respectively one- and two-dimensional magnetic states of matter. It is linear with spin-orbit coupling in contrast to the quadratic dependence associated with the unveiled non-local spin-mixing anisotropic MR (X-AMR). Such transport effects are systematized on various non-collinear magnetic states – spin-spirals and skyrmions – and compared to the uncovered spin-orbit-independent multi-site magnetoresistances. Owing to their simple implementation in readily available reading devices, the proposed magnetoresistances offer exciting and decisive ingredients to explore with all-electrical means the rich physics of topological and chiral magnetic objects.

<sup>&</sup>lt;sup>1</sup> Peter Grünberg Institut and Institute for Advanced Simulation, Forschungszentrum Jülich and JARA, D-52425 Jülich, Germany. <sup>2</sup> Faculty of Physics, University of Duisburg-Essen and CENIDE, 47053 Duisburg, Germany. <sup>⊠</sup>email: i.lima.fernandes@fz-juelich.de; s.lounis@fz-juelich.de

he electrical reading of information carriers defines the viability of prospected paradigm shifts for future data storage media and logic circuits. Ideal candidates are topological magnetic textures such as individual skyrmions<sup>1,2</sup> due to their inherent stability<sup>3-5</sup> and swift manipulation by currents of very low density<sup>1,6-10</sup> or electric field<sup>11,12</sup>. A successful implementation in available technologies hinges on the electrical detection of the chiral nature of these objects and on the ability to discern distinct topological spin entities, which can coexist in a given device<sup>13–22</sup>. Over the last years, control of spin-chirality, settled by the direction of the Dzyaloshinskii-Moriva interaction (DMI)<sup>23,24</sup>, was demonstrated experimentally. For instance, reversible chirality transition was realized via hydrogen chemisorption and desorption<sup>25</sup> while the application of an electric field or ultrashort electromagnetic pulse induce large modifications of DMI<sup>26,27</sup> in accordance with theoretical predictions<sup>22,28,29</sup>.

Identifying the vector spin-chirality, which is defined by the cross-product of adjacent magnetic moments is pertinent when addressing one-dimensional magnetic states such as spin-spirals and domain walls. This notion is, however, complemented with concepts such as helicity  $\gamma$  and topological charge Q when dealing with two-dimensional spin-textures<sup>5</sup> (see Fig. 1a-f and Supplementary Note 1). Q measures the wrapping of the magnetization around a unit sphere and enables to discern skyrmions (Q = -1)from antiskyrmions (Q = 1) or magnetic vortices (Q = 0.5).  $\gamma$  is defined by the in-plane magnetic moments swirling direction (e.g., clockwise or counterclockwise) and distinguishes magnetic textures of identical topological charge such as Bloch- from Néeltype skyrmions. While Néel-type skyrmions exhibit a righthanded or left-handed cycloidal spin rotation leading to a helicity of y = 0 or  $y = \pi$ , respectively, Bloch-type skyrmions host helical spin rotation with a helicity of  $y = \pm \pi/2$ .

Electric readout of chirality has rarely been possible with conventional technologies based on current perpendicular-toplane (CPP) geometries. Resting on tunnel magnetoresistance (TMR), which requests two magnetic electrodes, spin-polarized scanning tunneling microscopy/spectroscopy (STM/STS) was so far the only technique successful in detecting the chirality of spin spirals and sub-10 nm skyrmions<sup>30-35</sup>. The challenge resides in the highly non-trivial full control of the magnetization direction of the readout electrode and the sensing efficiency, dictated by the relative alignment of the magnetization of two electrodes. Obviously, the realization of all-electrical chiral detection, i.e., readout with a non-magnetic electrode, would enable a remarkable leap forward on the basis of a robust practical implementation. However, the known MR effects such as the anisotropic MR (AMR)<sup>36–39</sup> and the recently discovered highly efficient spin-mixing MR (XMR)<sup>40,41</sup> are expected to be transparent to the main attributes of topological structures: chirality or helicity. With an efficiency of a few percent, the AMR originates from spin-orbit coupling (SOC) and is by nature an on-site effect that depends on the local quantization axis of the magnetization relative to the crystal lattice. The X in XMR stands for spinmixing since the XMR effect has been proposed to mainly arise from the spin-mixing of the electronic states as a result of a nonlocal mechanism driven by electron scattering at atoms having canted magnetic moments independently from SOC40,41. Intriguingly, the precise nature of the dependence of measured signals on the opening angles of the underlying spin-textures remained so far elusive42.

In contrast to CPP geometries, all-electrical chiral and topological characterization is in principle possible with current-inplane (CIP) transport concepts such as the topological Hall effect<sup>43</sup> or the recently proposed chiral<sup>44</sup> and non-collinear<sup>45</sup> Hall

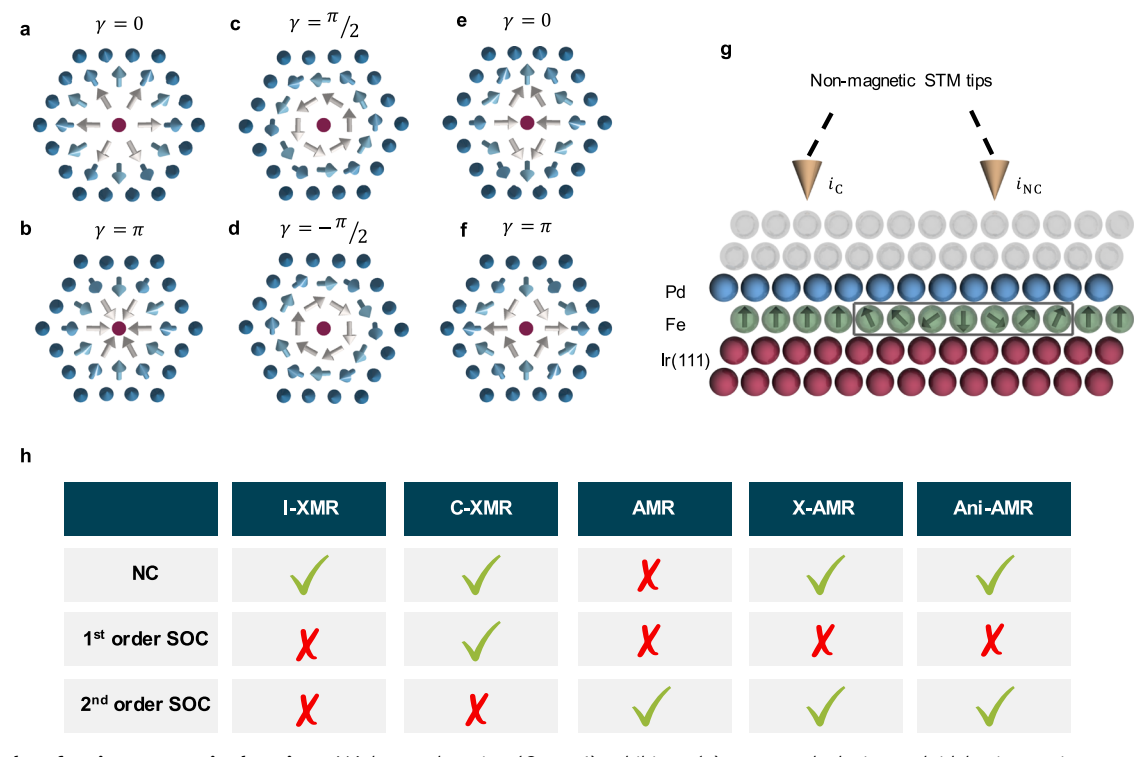


**Fig. 1 Examples of various magnetic skyrmions.** Néel-type skyrmion (Q = -1) exhibits a **(a)** counter-clockwise cycloidal spin rotation, e.g,  $\gamma = \pi$ . The Bloch skyrmion exhibits a helical spin rotation with helicity a **(c)**  $\gamma = \pi/2$  or **(d)**  $\gamma = -\pi/2$ . The antiskyrmion (Q = 1) with helicity **(e)**  $\gamma = 0$  and **(f)**  $\gamma = \pi$ . **g** Illustrative STS experiment detecting the electronic signals emanating from either a magnetic skyrmion or the ferromagnetic background. The sample consists of fcc-Pd (blue spheres) atop an Fe overlayer (green spheres) on single-crystal fcc-lr(111) bulk substrate (red spheres). The tip probes the local density of states (LDOS) two vacuum layers (gray spheres) away from Pd. **h** Classification of the different unveiled magnetoresistances as function of triggering mechanisms: non-collinear (NC) magnetism, 1st and 2nd order SOC.

effects. However, these effects are fairly small in general and have to be disentangled from a large Hall background. Moreover, the required Hall bar junction complicates their integration in standard device structures  $^{46-50}$ .

In this work, we unveil the existence of a rich family of MR effects enabling the all-electrical perpendicular readout of distinct chirality or helicity characteristics of spin-textures. We utilize multiple scattering concepts and intensive systematic first-principles simulations of atomically resolved transport measurements as probed within STM/STS on magnetic textures generated in a prototypical material: fcc-PdFe bilayer deposited on Ir(111) surface (see Methods). The chosen substrate is well known<sup>31,32,40,51–53</sup> to host isolated Néel-type skyrmions with a few nanometers diameter.

The discovered set of MRs are categorized in terms of the presence (or not) of non-collinear magnetism, SOC and their concomitant intertwining, as schematically illustrated in Fig. 1h. Purely non-collinear magnetism, i.e., without SOC, gives rise to an isotropic MR induced by the spin-mixing of electronic states due to the misalignment of the atomic magnetic moments, which is the transport phenomenon usually discussed in Refs. 40,41. We name it here I-XMR since it is isotropic and transparent to SOC related phenomena, as shown from our analytical derivations and systematic ab-initio simulations. We identify the MR chiral in nature, the chiral XMR effect (C-XMR), which is linear in SOC and requires non-collinear magnetism as well as broken inversion symmetry similarly to the conditions giving rise to DMI. C-XMR reaches large efficiencies permitting to distinguish and spatially probe the chiral nature of a given magnetic object. Traditional AMR is quadratic in SOC and emerges in a collinear magnetic environment upon a global rotation of the spin moments. In our study, however, we found a spin-mixing AMR (X-AMR) effect, which is also quadratic in SOC but it is non-local and depends on the canting angle between magnetic moments. In contrast to AMR, its magnitude can be as large as conventional MR efficiencies. The peculiar angular and spatial dependencies characterizing each of the different MR mechanisms enable their straightforward experimental detection and project a plethora of opportunities for basic and applied research of chiral and topological magnets.

# Results

Impact of helicity on the XMR signal. According to the Tersoff–Hamann model  $^{54}$ , the local density of states (LDOS) decaying from a particular site i into the vacuum is proportional to the differential conductance dI/dV at a bias voltage  $V_{\rm bias}$  relative to the highest occupied state of the sample measured with STM employing a non-magnetic tip. The latter is assumed in the second vacuum layer above the Pd substrate, as shown in Fig. 1g. The efficiency of the XMR effect is calculated as the ratio between the deviation of the conductance on top of a skyrmion from that of a reference point, which we choose to be the collinear magnetic region (see Methods section):

$$XMR^{y}(E) = \frac{LDOS_{NC}^{y}(E) - LDOS_{C}(E)}{LDOS_{C}(E)},$$
 (1)

where C and NC correspond to the collinear and non-collinear magnetic areas, respectively, as shown in Fig. 1, while  $\gamma$  indicates the helicity of the skyrmion.

As understood currently, the XMR effect results mainly from the non-collinearity of the magnetic moments without invoking spin-orbit coupling. The latter, however, can affect the measured XMR signal due to AMR. As aforementioned, both effects are chiral- or helicity-independent. This implies that XMR should be unaltered when switching the sense of rotation of the magnetic

moments. This particular scenario is investigated by comparing the energy-resolved XMR<sup>y</sup>ratios to the I-XMR one obtained by switching-off SOC, as illustrated in Fig. 2a. For a systematic comparison, the relative angles are maintained fixed to that obtained from full self-consistency of the skyrmion with v = 0. The sense of rotation of moments has been switched to realize the skyrmion with  $y = \pi$  (see Fig. 1a, b). The spectra were obtained on top of the core of a Néel-type skyrmion with diameter  $D_{\rm sk} \approx 2.2$  nm. While at first sight, the XMR $^{\gamma=0}$  and  $XMR^{y=\pi}$  signals seem to have a similar shape, they remarkably do not lay on top of each other. Taking as an example the tunneling energy of 1.27 eV (see dashed line in Fig. 2a), we find that SOC enhances  $XMR^{\gamma=\pi}$  by a factor of three in strong contrast to the drastic reduction and even change of sign imposed on XMRy=0. Such discrepancy is not limited to the core of the skyrmion but is a general effect, as demonstrated in the spatial maps plotted in Fig. 2c-e. The three maps are indeed very different, with the signal collected on XMR $^{\gamma=\pi}$  being the largest. At an energy of 0.61 eV (dot-dashed line in Fig. 2a), SOC seems now to reduce the XMR emanating from both skyrmions but favoring the observation of the skyrmion with helicity y = 0instead of the one with  $y = \pi$ . Impressively, the XMR signal without SOC peaks up at a value of ≈ 35%, but with SOC the XMR efficiency crashes down to  $\approx 24\%$  for  $\gamma = \pi$ . The patterns found for  $XMR^{\gamma=0,\pi}$  cannot be explained by the hitherto known mechanisms: merely SOC-independent non-collinear magnetism or chiral-insensitive AMR. Overall, this evidences the existence of new MR effects at play.

The alteration of the XMR signals results certainly from the change in the electronic structure imposed by the reversal of the skyrmion's helicity as illustrated in Fig. 2b, where a comparison is displayed between the LDOS measured on top of the skyrmionic (core) and collinear configurations. For the particular bias voltages addressed earlier, SOC reduces the predicted dI/dV amplitude at 0.61 eV and enhances at 1.27 eV the signal pertaining to the skyrmion with  $\gamma=\pi$  without affecting that of the zero-helicity skyrmion. In general, the shape, linewidth, and energy of the electronic states depend simultaneously on SOC and on the chirality of the underlying magnetic configuration. Clearly, SOC enables electronic hybridization channels sensitive to the sense of rotation of the magnetic moments.

Multi-site isotropic, chiral, and anisotropic XMR signals. A deeper understanding of the unveiled observations can be unraveled by scrutinizing the different contributions to the LDOS, which are enabled by the rotation of magnetic moments. In the process of building up the electronic structure at a given site, electrons scatter in the lattice and hope between neighboring magnetic atoms, picking up various information. Using multiple scattering theory (for details see Supplementary Information 2), we demonstrate that local and non-local multi-site contributions of different nature emerge: isotropic (independent from SOC), chiral (linearly dependent on SOC), and anisotropic achiral (quadratically dependent on SOC), which are strongly contingent to the underlying magnetic texture. We find that the all-electrical XMR signal at a site *i* is a sum of four terms:

$$XMR(E) = I-XMR(E) + C-XMR(E) + X-AMR(E) + Ani-XMR(E).$$
 (2)

We start with the most basic contribution, I-XMR, which is isotropic and does not require SOC. As shown in Supplementary Note 2, it primarily arises from a two-site isotropic term,  $\gamma_{\text{I-XMR}}(E) \, \mathbf{S}_i \cdot \mathbf{S}_j$ , which quantifies the change of the LDOS of atom i because of the misalignment of its moment from the one carried by a neighboring atom j independently from SOC. Although the coupling can in principle be long-ranged, we limit

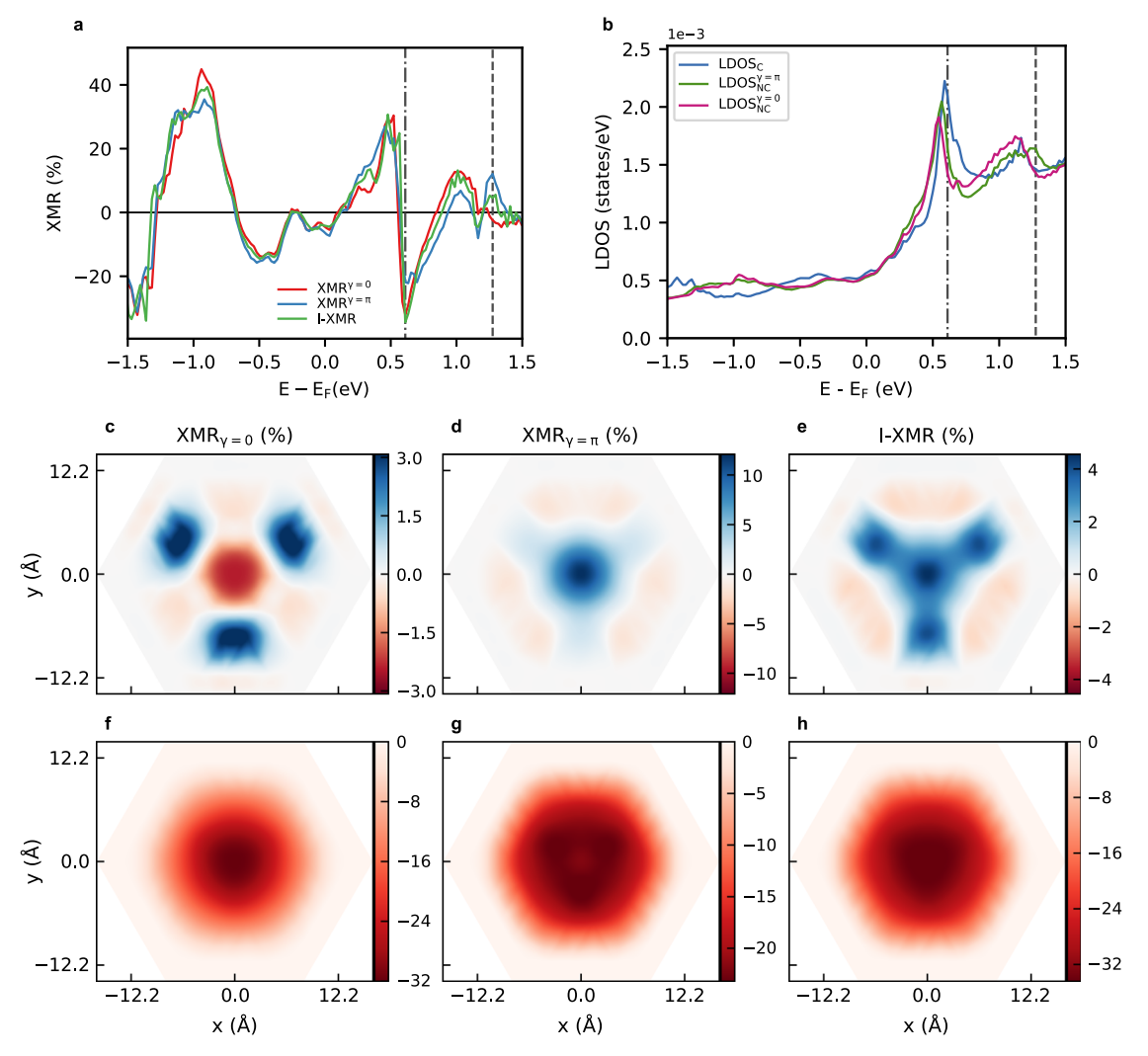


Fig. 2 Impact of the helicity on the XMR signal. a Comparison of energy-resolved XMR signals with different helicities and without SOC measured on top of the skyrmion's core. **b** Sum of spin-resolved electronic structure in the vacuum on top of the core of a Neéel-type skyrmion with diameter  $D_{\rm sk} \approx 2.2$  nm for different helicities and above the collinear configuration. The dashed and doted-dahed lines indicate, respectively, the tunneling energies  $eV_{\rm bias} = 1.27 \, eV$  and  $0.61 \, eV$  at which a spatial map of the whole skyrmion is plotted for **c**, **f** XMR $^{\gamma=0}$ , **d**, **g** XMR $^{\gamma=\pi}$  and **e**, **h** I-XMR signals.

our discussion here to nearest neighbors. This indicates that the magnetoresistance should change in a cosine fashion upon rotation of the moments, with a maximum expected when the moments are aligned antiferromagnetically. In the adiabatic approximation, i.e., when the skyrmions are large, it is then expected that the isotropic contribution should be quadratic with the rotation angle between two magnetic moments. Similarly to the extended Heisenberg Hamiltonian, one can identify an additional biquadratic contribution  $\gamma_{I-XMR}^{4-spin}(E)(\mathbf{S}_i\cdot\mathbf{S}_j)^2$  and even other higher-order terms.

Besides the isotropic contributions, we uncover a chiral term, C-XMR, linear with SOC and directly proportional to the chiral product between the spin-moment i and its neighboring moments:  $\gamma_{\text{CXMR}}(E) \hat{\mathbf{c}}_{ij} \cdot \left(\mathbf{S}_i \times \mathbf{S}_j\right)$ , where  $\hat{\mathbf{c}}$  is analogous to the DM vector and obeys therefore similar symmetry rules. Owing to the chiral nature of this term, rotating the moments clockwise or counter-clockwise modifies the LDOS in an opposite fashion. The largest contribution arises if the rotation angle is  $\pi/2$ . For large skyrmions, the angular dependence is linear with the angle between moments. Obviously, since the remaining contributing terms are achiral, by switching the helicity of the skyrmion (or the chirality of a spin-spiral or a domain wall), one can immediately

extract the chiral XMR:

$$C-XMR^{y=0}(E) = -C-XMR^{y=\pi}(E) = \frac{1}{2} \left( XMR^{y=0}(E) - XMR^{y=\pi}(E) \right).$$
 (3)

The usual AMR is quadratic in SOC and is local by nature since it only depends on the orientation of moment  $i^{36-39}$ . Conventionally, it is written as  $\gamma_{AMR}(E)(\mathbf{e}^{\mathbf{z}} \cdot \mathbf{S_i})^2$ , assuming that the anisotropy field responsible for the AMR effect points along the cartesian direction z. In our multiple scattering expansion, however, we uncover non-local (multi-site) dependencies generalizing the AMR to what we dub spin-mixing AMR (X-AMR) effect. The latter is proportional to  $\gamma_{X-AMR}(E)(\mathbf{e}^{\mathbf{z}} \cdot \mathbf{S_i})(\mathbf{e}^{\mathbf{z}} \cdot \mathbf{S_j})$ . So here, the angular dependence is  $\cos \theta_i \cos \theta_j$  instead of the expected local angular dependence  $\cos^2 \theta_i$ , where  $\theta_i$  is the polar angle pertaining to moment i. Furthermore, we find a SOC-correction to the isotropic two-site term:  $\gamma_{Ani-XMR}(E) \mathbf{S_i} \cdot \mathbf{S_i}$ .

Owing to the distinct angular dependence of each of the identified MRs, it is possible to fit the spatial maps and extract the magnetoresistance weights associated to each mechanism. We can expand Equation (2):  $XMR(E) = \sum_{i \neq j} XMR_{ij}(E)$  with the sum

Energy	2-spin <sup>y</sup> I-XMR	4-spin <sup>y</sup> I-XMR	γc-xmr	γamr	γx-amr	γ <sub>Ani-XMR</sub>
0.56	- 6.4190	0.0361	3.7392	-0.9416	4.7319	0.0107
0.61	12.4692	-0.1588	2.0918	0.7079	-3.3460	0.1750
1.27	-1.0456	0.0045	3.1518	0.0206	0.0442	-0.0443

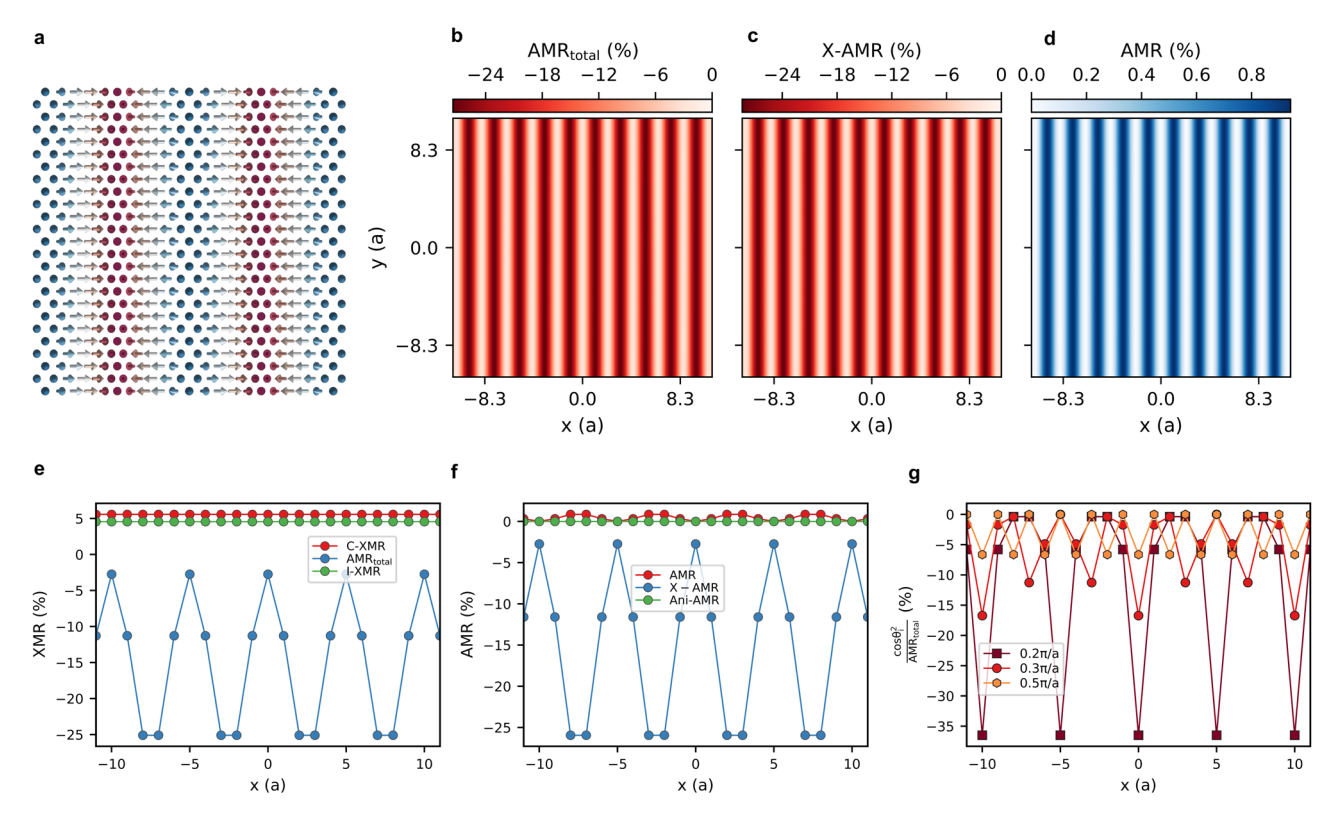


Fig. 3 Magnetoresistance patterns characterizing spin-spirals. a Spin-spiral with wave vector  $q = 0.2 \,\pi/a$  along the [100] direction, with a being the inplane lattice constant of Ir(111), i.e.,  $a = a_{\text{bulk}}/\sqrt{2}$  where  $a_{\text{bulk}} = 3.83 \,\text{Å}$ , and associated AMR signals: **b** total AMR, **c** X-AMR, and **d** conventional AMR considering the MR weights obtained at a bias energy of  $eV_{\text{bias}} = 0.56 \,\text{eV}$ . A systematic comparison of the different XMR components along the x-direction is provided in (**e**, **f**). The ratio  $\cos^2\theta_i/\text{AMR}_{\text{total}}$  is shown in (**g**) for spirals of wave vectors  $0.2 \,\pi/a$ ,  $0.3 \,\pi/a$ , and  $0.5 \,\pi/a$  to visualize the contribution of the new X-AMR.

limited to the nearest neighbors and :

$$\begin{aligned} \text{XMR}_{ij} &= \left[ \gamma_{\text{I-XMR}}^{\text{2-spin}} + \gamma_{\text{Ani-XMR}} \right] \mathbf{S}_i \cdot \mathbf{S}_j + \gamma_{\text{I-XMR}}^{\text{4-spin}} (\mathbf{S}_i \cdot \mathbf{S}_j)^2 \\ &+ \gamma_{\text{C-XMR}} \, \hat{\mathbf{c}}_{ij} \cdot \left( \mathbf{S}_i \times \mathbf{S}_j \right) + \gamma_{\text{X-AMR}} (\mathbf{e}^z \cdot \mathbf{S}_i) (\mathbf{e}^z \cdot \mathbf{S}_i), \end{aligned} \tag{4}$$

where the energy dependence is omitted for simplicity.

We expect the spatial map of each contribution to show distinctive patterns depending on the underlying spin-texture. The overlap of all terms can be complex and hinges on the MR weights magnitude and sign. In Table 1, we list the weight distributions for three bias energies: 0.56, 0.61, and 1.27 eV as obtained for the skyrmion studied in Fig. 2 (see Supplementary Note 3–5 for further details). One immediately remarks that all contributions can be of the same order of magnitude, with their sign and size being energy-dependent. We note that in contrast to the AMR weight, the contribution of the rest of the parameters will be enhanced due to the non-local nature of their associated MRs. On the fcc-111 surface, the maximum enhancement factor of 6 is expected due to the number of nearest neighboring pairs. Remarkably, the weight pertaining to X-AMR is larger than that

of the conventional AMR. Even if quadratic with SOC, it can directly compete with the weight characterizing C-XMR, which is linear with SOC. The SOC-independent XMR seems to provide the largest contribution to the electrical signal, however, the unveiled SOC-driven MRs are significant. We note that at 1.27 eV, the signal is dominated by C-XMR with a weight of opposite sign to the conventional I-XMR.

Before proceeding to the skyrmion case, it is instructive to explore the behavior of the different MRs for the case of a homogeneous spin-spiral (see Fig. 3) utilizing MR weights provided in Table 1 at an energy bias of  $eV_{\rm bias}=0.56\,{\rm eV}$ . We note that the PdFe bilayer on Ir(111) surface hosts spin spirals when the magnetic field is off. Since the rotation angle of the magnetic moments is constant, I-XMR, Ani-XMR, and C-XMR are not altered across the whole homogeneous spirals and can only be probed upon modification of the spin-spiral pitch (or size of a domain wall). If one manages to switch the chirality of the spiral with external means  $^{22,25-29}$ , C-XMR would change sign. In general, the spin-spiral patterns of the probed all-electrical MR emerge uniquely from both the AMR and X-AMR, summing up

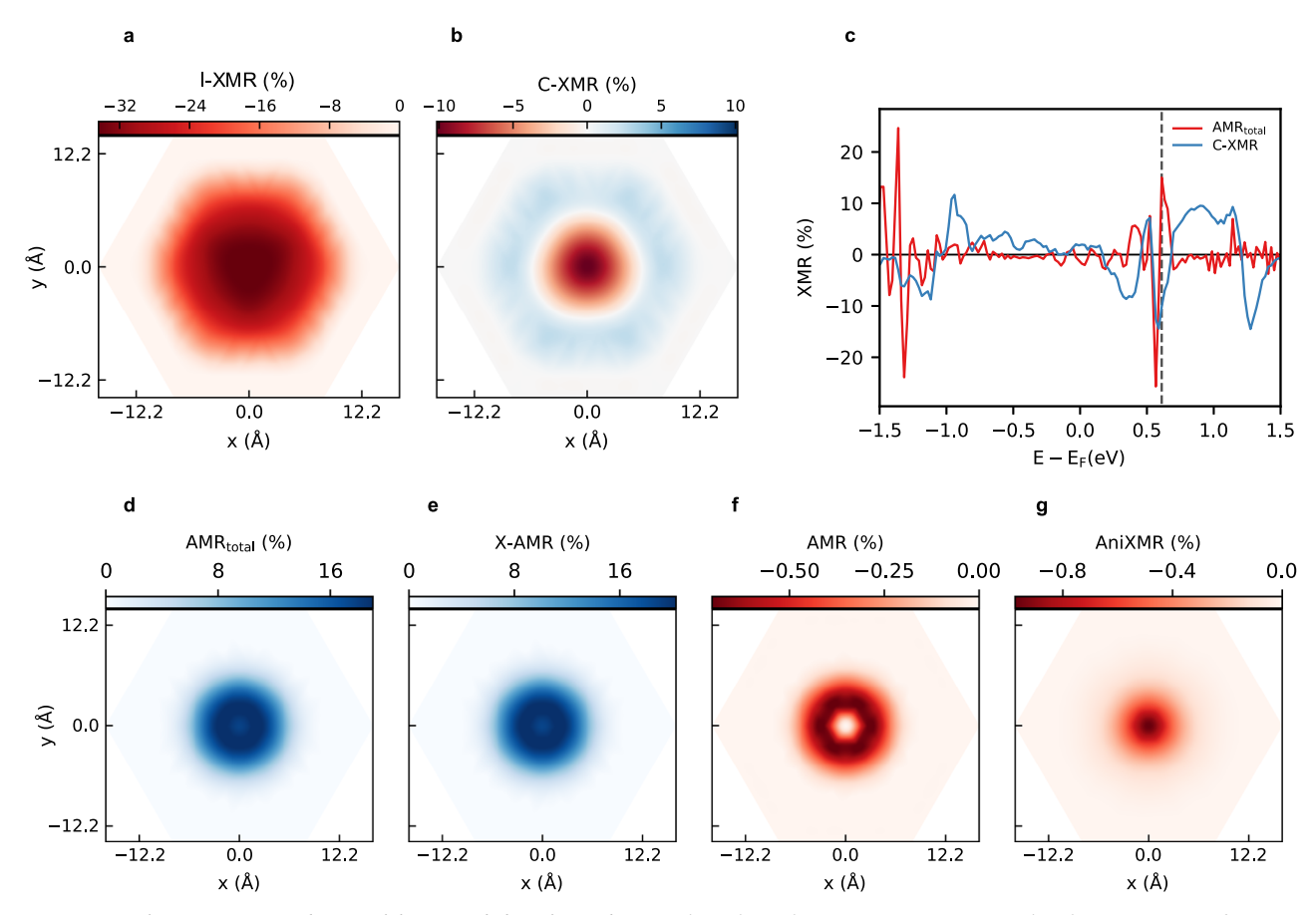


**Fig. 4 Magnetoresistance patterns characterizing a Néel skyrmion. a, b** Spin-orbit independent XMR pattern compared to the one emerging from C-XMR as obtained at the energy bias of  $eV_{bias} = 0.61 \, eV$ . **c** Comparison of the energy-resolved C-XMR and total AMR efficiencies measured atop the core of the skyrmion. The dashed line indicates the energy at which the two-dimensional maps are extracted. **d** Total AMR signal decomposed into the (**e**) X-AMR, (**f**) conventional AMR, and (**g**) ani-XMR components.

to the total AMR (Fig. 3e). At first sight, they look all similar (Fig. 3b–d), but a closer inspection of their angular dependence reveals differences owing to their local versus non-local nature (Fig. 3f). By dividing the conventional  $\cos^2(\theta)$  characterizing the traditional AMR by the total AMR, one can identify the signature of X-AMR as exemplified in Fig. 3g for different spiral pitches. Increasing the wave vector of the spiral enlarges the rotation angle of the magnetic moments, which enhances (diminishes) the contribution of the X-AMR (conventional AMR). The latter provides a well-defined path for the experimental detection of X-AMR.

In contrast to spin-spirals, skyrmions are inhomogenous spintextures that trigger spatial modulations of all XMR components. This is visualized in Fig. 4 for the various MR patterns hosted by a Néel skyrmion at 0.61 eV (see Supplementary Note 6 for the MR patters of different skyrmionic structures). The dissimilarity of the shape, extension, and sign of the plotted efficiencies is remarkable. On the one hand, the C-XMR and I-XMR culminate to their maximum value (respectively -10.2% and -34.4%) at the skyrmion core (Fig. 4a, b). On the other hand, C-XMR experiences a change of sign close to the skyrmion's edge, contrary to I-XMR. Interestingly, the total AMR contrast is positive and narrower than the negative ones obtained for I-XMR and C-XMR (Fig. 4d). Keeping in mind that the sign of C-XMR switches with the change of helicity, this is a nice example demonstrating how different MRs can counter-act each other when reading chiral magnetic objects. The total AMR signal exhibits a maximum of 19% slightly off-centered from the skyrmion's core. At the latter location, the total AMR value drops down to 17.6%, which is expected to be zero, i.e., similar to that of the ferromagnetic background, when counting only on the traditional local AMR. In this particular case, the non-local contribution X-AMR, which is two orders of magnitude larger than the conventional AMR or the Ani-XMR (Fig. 4e–g), dominates the total AMR efficiency. While at 0.61 eV the SOC-driven signals, i.e., C-XMR and total AMR, are equally important, albeit different sign, we identify in Fig. 4c the energy window ranging from 0.7 to 1.4 eV where the MR is mostly of chiral origin. At about — 1.36 eV, the total AMR dominates the scene by reaching an impressive efficiency of 24.7%.

Other chiral spin textures. For completeness, we have expanded our investigations to other skyrmionic structures such as Bloch skyrmions and antiskyrmions (Fig. 5d-f). Henceforth, we focus on the C-XMR effect, which is a primary tool to distinguish chiral spin textures. We assume the anisotropy fields associated with the Néel skyrmion of zero helicity and plot in Fig. 5a-c the spatial C-XMR patterns at 1.27 eV. On the one hand, the C-XMR of the Néel-type skyrmion is isotropic, reaches a maximum value at its core, and reduces in magnitude when approaching the edge. On the other hand, the C-XMR patterns obtained for the Bloch-type skyrmions and antiskyrmions are strongly anisotropic with offcentered maxima, reflecting their chiral texture as described by  $\hat{\mathbf{c}}_{ii} \cdot (\mathbf{S}_i \times \mathbf{S}_i)$ . Here regions of zero C-XMR arise within the skyrmionic area contrary to what is observed in Néel skyrmions. In the Bloch skyrmion, one finds a sequence of six large-amplitude lobs separated by zero-lines whenever the chiral signal changes

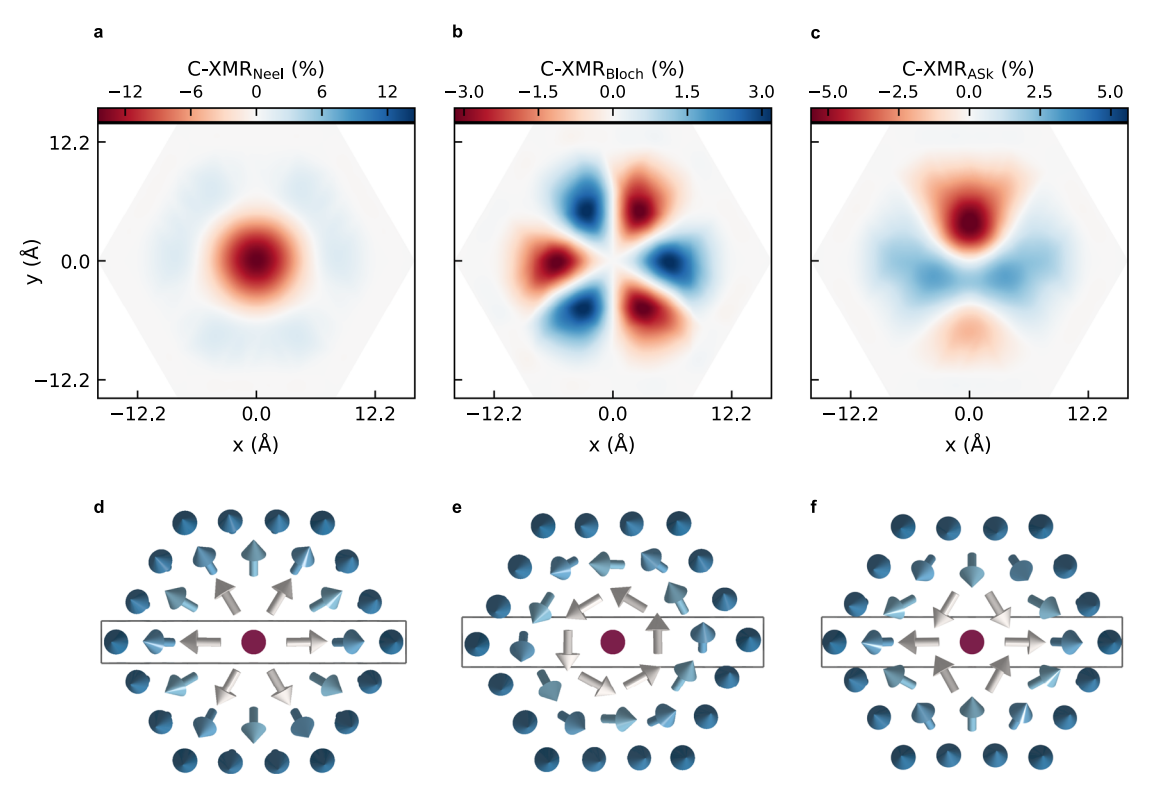


Fig. 5 C-XMR signals on various chiral skyrmions. On the upper panel the C-XMR signal at a bias energy of  $eV_{bias} = 1.27 eV$  is shown for (a) Néel type and (b) Bloch type skyrmions and for (c) antiskyrmions. On the lower panel **d-f** the corresponding skyrmion magnetic textures with diameter  $D_{sk} \approx 2.2 \text{ nm}$  are shown. The rectangular boxes are used in the text to address the change of chirality across the different skyrmions.

sign. In this particular case, the dot product of spin-chirality vector and the underlying DMI vector switches within each row of atoms when passing across the skyrmion's core (see the box shown in Fig. 5f). This explains the emergence of lobs of opposite sign facing each other, which surround the central region that carries a vanishing signal due to the perfect cancellation of chiral contributions. In the antiskyrmion case, one notices four lobs: two of positive sign merging atop the skyrmion core, which separate the two lobs carrying negative chiral contrast. Here the spin-chirality along the x-axis passing through the core of the skyrmion is of opposite sign than that along the y-axis. Surprisingly, the symmetry characterizing the antiskyrmion is not transmitted to the C-XMR signal: The upper (left) half part is different from the lower (right) one. This originates from the electronic contribution of the Pd overlayer, where the atoms sit on a triangular lattice following the ABC stacking characterizing the assumed fcc(111) surface.

### **Discussion**

The chirality or topological nature of spin-textures plays a crucial role in determining their physical properties as well as their potential practical use. Those aspects are difficult to address with current readout technologies based on the CPP geometries. Here, we discovered a rich family of spin-mixing magnetoresistances that enables an all-electrical reading of non-collinear magnetic states. Based on systematic first-principles simulations and multiple scattering based concepts, we demonstrated the existence of a highly efficient chiral spin-mixing magnetoresistance, linear with SOC and directly induced by the chiral nature of the underlying spin-texture. We uncovered the contributions of terms quadratic with SOC that give rise to the conventional local anisotropic magnetoresistance and the newly found non-local anisotropic magnetoresistance. The latter is found to be orders of

magnitude larger than the conventional anisotropic magnetoresistance and competes directly with the chiral or SOC-independent spin-mixing magnetoresistance in shaping the final electrical signal. The patterns emerging from each of the unveiled magnetoresistance terms as well as their distinct dependence on the misalignment of the magnetic moments can be utilized to identify their respective amplitude and probably explain previously reported intriguing behaviors<sup>41</sup>.

We envisage the scenario of topological spin-textures driven in a racetrack equipped with a non-magnetic detecting electrode, which can either offer atomic resolution, as possible with an STM tip, or not as it is the case in more conventional CPP devices (see Fig. 6). STM enables the atom-by-atom exploration of the signal dependence on the angles between the magnetic moments. Currently, in such experiments, the measured spectra are deconvoluted assuming dependencies expected from TMR (if the tip is magnetic), AMR and XMR but assuming for the latter that the signal is directly proportional to the angle between adjacent moments. Our findings demonstrate that the contributing phenomena are richer than assumed so far and clearly lead to complex interference patterns, which can be disentangled owing to the distinctive simple dependencies of each of the contributing effects on the direction of the magnetic moments. This is analog to the procedure followed when dissecting Hall signals in transversal resistivity measurements. The overall signal can include the anomalous, topological, and quantum Hall effects besides the ordinary one. The different effects have a distinct origin, each signaling very different physics. They do interfere and it is only through their specific dependence with respect to various parameters, such as the magnetic field and magnetization direction, that one can extract them and make conclusions on important physics of the probed materials.

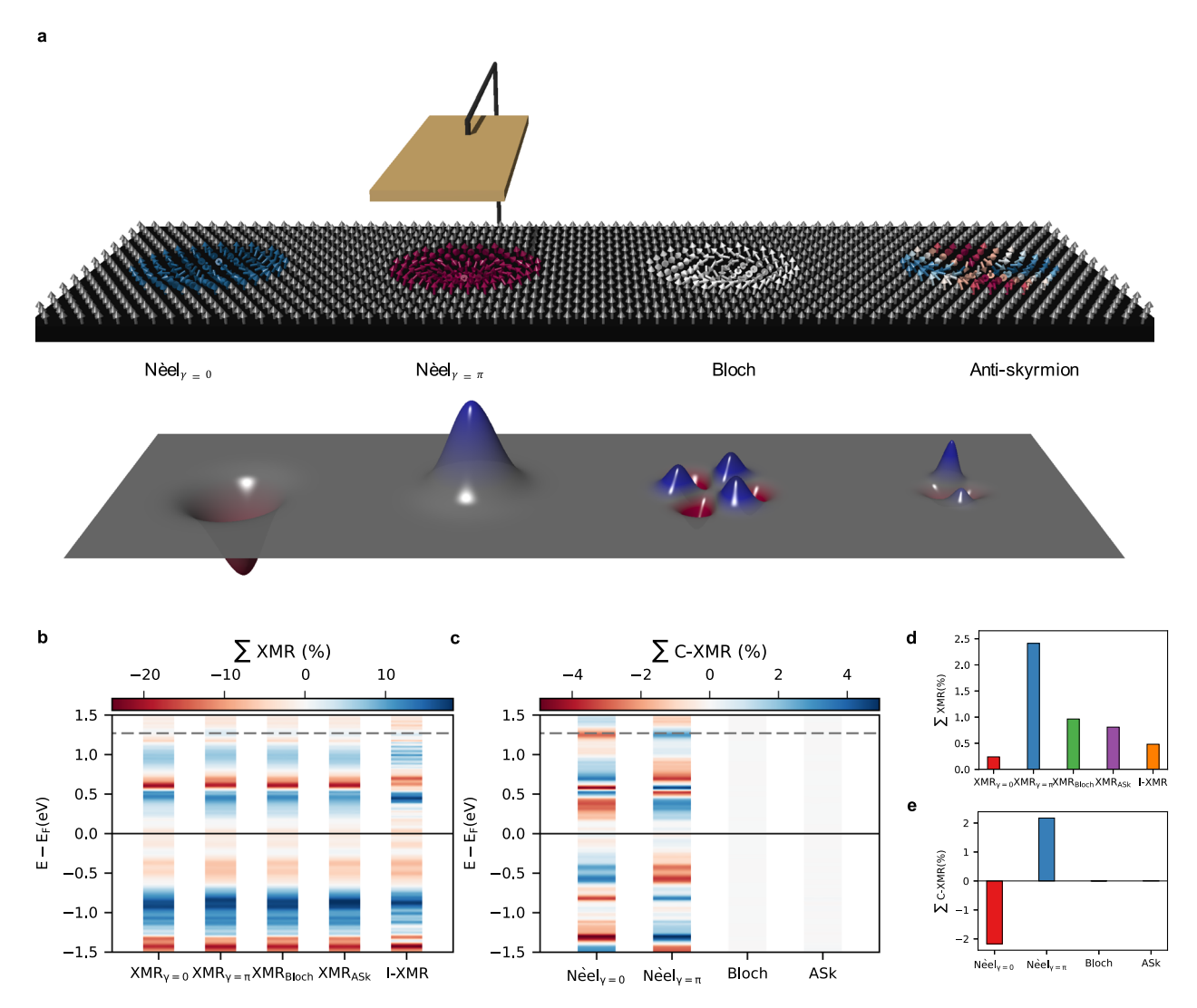


**Fig. 6 Concept for all-electron detection of various skyrmions passing in a racetrack device. a** If the electrode provides atomic resolution, the C-XMR shows very distinct profiles as obtained at the tunneling energy  $eV_{bias} = 1.27 \text{ eV}$ . Note the sign change for Néel skyrmions of opposite helicity. **b, c** If the electrode lacks atomic resolution, the detected signal is collected over the area encompassing the skyrmion. The bias-resolved signal is plotted for the total XMR, I-XMR, and C-XMR signals. **d, e** show a comparison of the total XMR and C-XMR efficiencies obtained at  $eV_{bias} = 1.27 \text{ eV}$  (dashed lines in **b, c**).

In our context, the existence of spin spirals in materials hosting skyrmions permits to distinguish in the measured spectra the non-local anisotropic magnetoresistance X-AMR,  $\propto \cos\theta_i \cos\theta_j$  from the local one,  $\propto \cos^2\theta_i$ , where  $\theta_i$  is the polar angle associated with moment  $S_i$  (assuming an out-of-plane anisotropy field). On one hand, the C-XMR behaves like  $\hat{\mathbf{c}}_{ij} \cdot \mathbf{S}_i \times \mathbf{S}_j$ , which for small angles is proportional to the average angle between a given moment and its nearest neighbors, as extracted experimentally ( $\hat{\mathbf{c}}$  being the analog of the DM vector and obeys similar symmetry rules). As an example, Fig. 6a illustrates the C-XMR signals pertaining to different skyrmions (note the opposite sign for Néel skyrmions of different helicity). On the other hand, the I-XMR gives rise to a dot product dependence,  $S_i \cdot S_j$ .

If the detecting electrode lacks atomic resolution, one could rely on the total signal sensed from the underlying area encompassing the skyrmion. Here, the amplitude of the various MRs hinges on their respective origin and simultaneously on the size of the confined spin-textures, which can be controlled by an external magnetic field. To have an overview, Fig. 6b shows the biasresolved total XMR signal for different skyrmions which can be compared to that emanating from the I-XMR. In general, spatial

oscillations lead to interferences that affects the magnitude of the overall signal. One notices blue, red, and white bands corresponding to positive, negative, and transparent MR efficients, which are not identical for the different magnetic objects. The I-XMR, X-AMR and AMR being the same for the particular considered cases, the differences in the total XMR efficiency originates from the C-XMR due to the associated helicities. In Fig. 6d, e, one clearly sees that the skyrmions give rise to disparate total XMR induced by C-XMR, as obtained at a tunneling energy of  $eV_{\rm bias}$  = 1.27 eV. An overview of the bias-resolved total C-XMR is shown in Fig. 6c, where one notices that MR pertaining to the Bloch and antiskyrmions vanishes as a result of the competing oscillations (lobs) shown for example in Fig. 6a. This occurs due to the chiral vector  $\hat{\mathbf{c}}_{ij}$  associated with C-XMR, that does not match the directions of the DM vectors that should stabilize the Bloch and antiskyrmions.

Overall, the unveiled phenomena enforce our view that such reading mechanisms represent a new avenue for further fundamental studies of the very rich physics of chiral and topological magnetism. We envision the use of the new magnetoresistances in readily available all-electrical readout device architectures to sense, distinguish and categorize the ever increasing number of predicted and discovered non-collinear spin-textures.

#### Methods

**Computational details.** The simulations are based on density functional theory (DFT) in the local spin density approximation as implementd in the full-potential scalar-relativistic Korringa-Kohn-Rostoker (KKR) Green function method with spin-orbit coupling included self-consistently<sup>55,56</sup>. The method enables the embedding of single magnetic skyrmions in a real-space approach that does not require the use of periodic supercells. The approach is based on two steps: First, self-consistent calculations of the skyrmion-free ferromagnetic slab with periodic boundary conditions are performed. The associated Green function,  $G_0$ , is extracted and utilized to solve the Dyson equation, schematically written as  $G = G_0 + G_0 \Delta V G$ , in order to obtain the new Green function G.  $\Delta V$  represents the potential changed after injecting the magnetic skyrmion. The magnetic textures are obtained in a self-consistent fashion till convergence is achieved.

The PdFe bilayer on Ir(111) surface is simulated with a slab consisting of a layer of Pd atop Fe, which is deposited on 34 layers of Ir. We assumed an fcc-stacking for all layers with atomic positions obtained from ab-initio  $^{51}$ . The embedded cluster consists of a total of 165 atoms, including 37 Fe atoms (see Refs.  $^{40,57-61}$  and references therein for details). We assume an angular momentum cutoff at  $l_{\rm max}=3$  for the orbital expansion of the Green function and when extracting the LDOS a k-mesh of  $200\times200$  is considered.

### **Data availability**

The data that support the findings of this study are provided in the Supplementary Information and in the main manuscript.

## Code availability

The KKR code is a rather complex ab-initio DFT-based code, which is in general impossible to use without proper training on the theory behind it and on the practical utilization of the code. We are happy to provide it upon request.

Received: 12 July 2021; Accepted: 1 March 2022; Published online: 24 March 2022

#### References

- Fert, A., Cros, V. & Sampaio, J. Skyrmions on the track. Nat. Nanotech. 8, 152–156 (2013).
- Fert, A., Reyren, N. & Cros, V. Magnetic skyrmions: advances in physics and potential applications. *Nat. Rev. Mater.* 2, 17031 (2017).
- Bogdanov, A. N. & Yablonskii, D. Thermodynamically stable "vortices" in magnetically ordered crystals. the mixed state of magnets. *J. Exp. Theor. Phys.* 95, 178 (1989).
- Rössler, U. K., Bogdanov, A. N. & Pfleiderer, C. Spontaneous skyrmion ground states in magnetic metals. *Nature* 442, 797–801 (2006).
- Nagaosa, N. & Tokura, Y. Topological properties and dynamics of magnetic skyrmions. Nat. Nanotech. 8, 899–911 (2013).
- Jonietz, F. et al. Spin transfer torques in MnSi at ultralow current densities. Science 330, 1648–1651 (2010).
- Sampaio, J., Cros, V., Rohart, S., Thiaville, A. & Fert, A. Nucleation, stability and current-induced motion of isolated magnetic skyrmions in nanostructures. *Nat. Nanotech.* 8, 839–844 (2013).
- Woo, S. et al. Observation of room-temperature magnetic skyrmions and their current-driven dynamics in ultrathin metallic ferromagnets. *Nat. Mater.* 15, 501–506 (2016).
- Jiang, W. et al. Direct observation of the skyrmion Hall effect. Nat. Phys. 13, 162–169 (2017).
- Litzius, K. et al. Skyrmion hall effect revealed by direct time-resolved x-ray microscopy. Nat. Phys. 13, 170–175 (2017).
- 11. Ma, C. et al. Electric field-induced creation and directional motion of domain walls and skyrmion bubbles. *Nano Letters* **19**, 353–361 (2018).
- Hu, J.-M., Yang, T. & Chen, L.-Q. Strain-mediated voltage-controlled switching of magnetic skyrmions in nanostructures. *Npj Computational Materials* 4, 1–7 (2018).
- Koshibae, W. & Nagaosa, N. Creation of skyrmions and antiskyrmions by local heating. *Nature Communications* 5, 5148 (2014).
- Leonov, A. O. & Mostovoy, M. Multiply periodic states and isolated skyrmions in an anisotropic frustrated magnet. *Nature Communications* 6, 8275 (2015).
- Ritzmann, U. et al. Trochoidal motion and pair generation in skyrmion and antiskyrmion dynamics under spin-orbit torques. *Nature Electronics* 1, 451–457 (2018).

- Rybakov, F. N. & Kiselev, N. S. Chiral magnetic skyrmions with arbitrary topological charge. *Phys. Rev. B* 99, 064437 (2019).
- Yokouchi, T. et al. Creation of magnetic skyrmions by surface acoustic waves. Nature Nanotechnology 15, 361–366 (2020).
- Ritzmann, U., Desplat, L., Dupé, B., Camley, R. E. & Kim, J.-V. Asymmetric skyrmion-antiskyrmion production in ultrathin ferromagnetic films. *Phys. Rev. B* 102, 174409 (2020).
- Jena, J. et al. Elliptical bloch skyrmion chiral twins in an antiskyrmion system. Nat. Commun. 11, 1–9 (2020).
- Gao, S. et al. Fractional antiferromagnetic skyrmion lattice induced by anisotropic couplings. Nature 586, 37–41 (2020).
- Heigl, M. et al. Dipolar-stabilized first and second-order antiskyrmions in ferrimagnetic multilayers. Nat. Commun. 12, 1–9 (2021).
- Yao, X., Chen, J. & Dong, S. Controlling the helicity of magnetic skyrmions by electrical field in frustrated magnets. *New Journal of Physics* 22, 083032 (2020).
- Dzyaloshinsky, I. A thermodynamic theory of "weak" ferromagnetism of antiferromagnetics. J. Phys. Chem. Sol. 4, 241–255 (1958).
- Moriya, T. Anisotropic superexchange interaction and weak ferromagnetism. *Phys. Rev.* 120, 91–98 (1960).
- Chen, G. et al. Observation of hydrogen-induced dzyaloshinskii-moriya interaction and reversible switching of magnetic chirality. *Physical Review X* 11, 021015 (2021).
- Srivastava, T. et al. Large-voltage tuning of dzyaloshinskii–moriya interactions: A route toward dynamic control of skyrmion chirality. *Nano Letters* 18, 4871–4877 (2018).
- Büttner, F. et al. Observation of fluctuation-mediated picosecond nucleation of a topological phase. *Nature Materials* 20, 30–37 (2021).
- Yang, H., Boulle, O., Cros, V., Fert, A. & Chshiev, M. Controlling dzyaloshinskii-moriya interaction via chirality dependent atomic-layer stacking, insulator capping and electric field. *Scientific Rep.* 8, 1–7 (2018).
- Desplat, L. et al. Dzyaloshinskii-moriya interaction induced by an ultrashort electromagnetic pulse: Application to coherent (anti)ferromagnetic skyrmion nucleation. arXiv preprint arXiv:2011.12055 (2020).
- Heinze, S. et al. Spontaneous atomic-scale magnetic skyrmion lattice in two dimensions. *Nat. Phys.* 7, 713–718 (2011).
- Romming, N. et al. Writing and deleting single magnetic skyrmions. Science 341, 636–639 (2013).
- Romming, N., Kubetzka, A., Hanneken, C., von Bergmann, K. & Wiesendanger, R. Field-dependent size and shape of single magnetic skyrmions. *Phys. Rev. Lett.* 114, 177203 (2015).
- Meyer, S. et al. Isolated zero field sub-10 nm skyrmions in ultrathin co films. Nat. Commun. 10, 3823 (2019).
- 34. Perini, M. et al. Electrical detection of domain walls and skyrmions in co films using noncollinear magnetoresistance. *Phys. Rev. Lett.* **123**, 237205 (2019).
- Muckel, F. et al. Experimental identification of two distinct skyrmion collapse mechanisms. Nat. Phys. 17, 395–402 (2021).
- McGuire, T. & Potter, R. Anisotropic magnetoresistance in ferromagnetic 3d alloys. IEEE Trans. Magn. 11, 1018–1038 (1975).
- Bode, M. et al. Magnetization-direction-dependent local electronic structure probed by scanning tunneling spectroscopy. *Phys. Rev. Lett.* 89, 237205 (2002)
- Gould, C. et al. Tunneling anisotropic magnetoresistance: A spin-valve-like tunnel magnetoresistance using a single magnetic layer. *Phys. Rev. Lett.* 93, 117203 (2004).
- Matos-Abiague, A. & Fabian, J. Anisotropic tunneling magnetoresistance and tunneling anisotropic magnetoresistance: Spin-orbit coupling in magnetic tunnel junctions. *Phys. Rev. B* 79, 155303 (2009).
- Crum, D. M. et al. Perpendicular reading of single confined magnetic skyrmions. Nat. Commun. 6, 8541 (2015).
- Hanneken, C. et al. Electrical detection of magnetic skyrmions by tunnelling non-collinear magnetoresistance. *Nat. Nanotechnol.* 10, 1039 (2015).
- Kubetzka, A., Hanneken, C., Wiesendanger, R. & von Bergmann, K. Impact of the skyrmion spin texture on magnetoresistance. *Phys. Rev. B* 95, 104433 (2017).
- Bruno, P., Dugaev, V. K. & Taillefumier, M. Topological hall effect and berry phase in magnetic nanostructures. *Phys. Rev. Lett.* 93, 096806 (2004).
- Lux, F. R., Freimuth, F., Blügel, S. & Mokrousov, Y. Chiral hall effect in noncollinear magnets from a cyclic cohomology approach. *Phys. Rev. Lett.* 124, 096602 (2020).
- Bouaziz, J., Ishida, H., Lounis, S. & Blügel, S. Transverse transport in twodimensional relativistic systems with nontrivial spin textures. *Phys. Rev. Lett.* 126, 147203 (2021).
- 46. Neubauer, A. et al. Topological hall effect in the *a* phase of mnsi. *Phys. Rev. Lett.* **102**, 186602 (2009).
- Lee, M., Kang, W., Onose, Y., Tokura, Y. & Ong, N. P. Unusual hall effect anomaly in mnsi under pressure. *Phys. Rev. Lett.* 102, 186601 (2009).

- Zhang, S. F. et al. Highly efficient domain walls injection in perpendicular magnetic anisotropy nanowire. Scientific Rep. 6, 24804 (2016).
- Maccariello, D. et al. Electrical detection of single magnetic skyrmions in metallic multilayers at room temperature. Nat. Nanotechnol. 13, 233 (2018).
- Zeissler, K. et al. Discrete hall resistivity contribution from néel skyrmions in multilayer nanodiscs. *Nat. Nanotechnol.* 13, 1161–1166 (2018).
- Dupé, B., Hoffmann, M., Paillard, C. & Heinze, S. Tailoring magnetic skyrmions in ultra-thin transition metal films. *Nat. Commun.* 5, 4030 (2014).
- Simon, E., Palotás, K., Rózsa, L., Udvardi, L. & Szunyogh, L. Formation of magnetic skyrmions with tunable properties in PdFe bilayer deposited on Ir (111). Phys. Rev. B 90, 094410 (2014).
- dos Santos Dias, M., Bouaziz, J., Bouhassoune, M., Blügel, S. & Lounis, S. Chirality-driven orbital magnetic moments as a new probe for topological magnetic structures. *Nat. Commun.* 7, 13613 (2016).
- Tersoff, J. & Hamann, D. Theory and application for the scanning tunneling microscope. *Phys. Rev. Lett.* 50, 1998 (1983).
- Papanikolaou, N., Zeller, R. & Dederichs, P. H. Conceptual improvements of the KKR method. J. Phys. Condens. Matter 14, 2799 (2002).
- Bauer, D. S. G. Development of a relativistic full-potential first-principles multiple scattering green function method applied to complex magnetic textures of nano structures at surfaces. PhD dissertation at the RWTH-Aachen (2013).
- Lima Fernandes, I., Bouaziz, J., Blügel, S. & Lounis, S. Universality of defectskyrmion interaction profiles. *Nat. Commun.* 9, 4395 (2018).
- Fernandes, I. L., Bouhassoune, M. & Lounis, S. Defect-implantation for the allelectrical detection of non-collinear spin-textures. *Nat. Commun.* 11, 1–9 (2020).
- Fernandes, I. L., Chico, J. & Lounis, S. Impurity-dependent gyrotropic motion, deflection and pinning of current-driven ultrasmall skyrmions in PdFe/Ir(111) surface. Journal of Physics: Condensed Matter https://doi.org/10.1088/1361-648X/ab9cf0 (2020).
- Arjana, I. G., Lima Fernandes, I., Chico, J. & Lounis, S. Sub-nanoscale atomby-atom crafting of skyrmion-defect interaction profiles. *Scientific Rep.* 10, 14655 (2020).
- Bouhassoune, M. & Lounis, S. Friedel oscillations induced by magnetic skyrmions: From scattering properties to all-electrical detection. Nanomaterials 11 https://www.mdpi.com/2079-4991/11/1/194 (2021).

#### **Acknowledgements**

This work is supported by the European Research Council (ERC) under the European Union's Horizon 2020 research and innovation program (ERC-consolidator grant 681405- DYNASORE and Grant No. 856538, project "3D MAGiC") and the Deutsche Forschungsgemeinschaft (DFG) through SPP 2137 "Skyrmionics" (Projects LO 1659/8-1, BL 444/16-2). We acknowledge the computing time granted by the JARA-HPC

Vergabegremium and VSR commission on the supercomputers JURECA at Forschungszentrum Jülich and at the supercomputing center of RWTH Aachen University.

#### Author contributions

S.L. initiated, designed, and supervised the project. I.L.F. performed the first-principles calculations and post-processed the data. S.L. provided the analytical derivations of the various magnetoresistance effects. I.L.F., S.B., and S.L. discussed the results and helped writing the manuscript.

#### **Competing interests**

The authors declare no competing interests.

#### Additional information

**Supplementary information** The online version contains supplementary material available at https://doi.org/10.1038/s41467-022-29237-0.

**Correspondence** and requests for materials should be addressed to Imara Lima Fernandes or Samir Lounis.

**Peer review information** *Nature Communications* thanks the anonymous reviewer(s) for their contribution to the peer review of this work.

Reprints and permission information is available at http://www.nature.com/reprints

**Publisher's note** Springer Nature remains neutral with regard to jurisdictional claims in published maps and institutional affiliations.



**Open Access** This article is licensed under a Creative Commons Attribution 4.0 International License, which permits use, sharing,

adaptation, distribution and reproduction in any medium or format, as long as you give appropriate credit to the original author(s) and the source, provide a link to the Creative Commons license, and indicate if changes were made. The images or other third party material in this article are included in the article's Creative Commons license, unless indicated otherwise in a credit line to the material. If material is not included in the article's Creative Commons license and your intended use is not permitted by statutory regulation or exceeds the permitted use, you will need to obtain permission directly from the copyright holder. To view a copy of this license, visit <a href="https://creativecommons.org/licenses/by/4.0/">https://creativecommons.org/licenses/by/4.0/</a>.

© The Author(s) 2022